Comparison of a bottom-up and a top-down approach for the creation of contact openings in a multi-stack oxide layer at the front interface of Cu(In,Ga)Se$_2$

Dilara G. Buldu[a,b,c,*], Jessica de Wild[a,b,c], Thierry Kohl[a,b,c], Gizem Birant[a,b,c], Guy Brammertz[a,b,c], Marc Meuris[a,b,c], Jef Poortmans[a,b,c,d,e], and Bart Vermang[a,b,c]

[a]Institute for Material Research (IMO), Hasselt University (partner in Solliance), Wetenschapspark 1, Diepenbeek 3590,Belgium

[b]Imec division IMOMEC(partner in Solliance), Wetenschapspark 1, Diepenbeek 3590, Belgium

[c]Energyville, Thor Park Genk 8320, Genk 3600, Belgium

[d]imec (partner in Solliance), Kapeldreef 75, Leuven 3001, Belgium

[e]Department of Electrical Engineering, KU Leuven, Kasteelpark Arenberg 10, Heverlee 3001, Belgium

[*]*Corresponding author.*
E-mail address: dilara.gokcen.buldu@imec.be (D. G. Buldu)

Abstract

The implementation of an oxide layer with contact openings to the Cu(In,Ga)Se$_2$ (CIGS) interfaces has become especially popular to reduce the recombination losses, resulting in a higher open-circuit voltage. While implementing this approach on the back surface is straightforward, it is more complicated for the front surface due to the roughness of the absorber as well as material selection constraints imposed by further processing steps. In this contribution, an AlO$_x$/HfO$_x$ multi-stack oxide layer with contact openings is applied between the CIGS and CdS layers. Two different approaches to create contact openings in multi-stack oxide layer are presented, and their advantages and disadvantages are investigated. In the bottom-up approach (BU), a NaCl salt pattern is created on the CIGS absorber surface, while in the top-down approach (TD), the pattern is created on the AlO$_x$ layer surface. Time-resolved photoluminescence (TR-PL) shows that the multi-stack design improves the PL decay time regardless of the approach, but when the CdS layer is deposited, the PL decay time decreases. A more severe decrease is observed in case of the BU approach. Capacitance-Voltage measurements show that there is no impact on doping level when the NaCl pattern is created on an AlO$_x$ surface. This work shows that any oxide material, even if not chemically resistant to the chemical bath deposition, can be applied at the CIGS/buffer layer interface, and additionally, any template can be used to create contact openings while preventing interaction between the material used for patterning and the CIGS, using the TD approach.

Keywords: Cu(In,Ga)Se$_2$ (CIGS); solar cells; front interface; Al$_2$O$_3$ and HfO$_2$; Bottom-up approach; top-down approach.

1.Introduction

The latest world record in the efficiency of Cu(In,Ga)Se$_2$ (CIGS) solar cell is over 23% (Nakamura et al., 2019). This high device efficiency was achieved with heavy alkali post deposition treatment (PDT) and a chemical bath deposited Zn(O,S) buffer layer (Nakamura et al., 2019). Nevertheless, a low open-circuit voltage (Voc) is still one of the most limiting parameters when trying to reach a higher efficiency. Recombination in the bulk and at the rear/front interfaces is the primary reason of the Voc loss in the device. To counteract this problem, in most cases, a bandgap graded-CIGS absorber is used to reduce the recombination at the rear/front interfaces (Nakada, 2012). However, as discussed in (Ochoa et al., 2020), the

tuning and controlling of the bandgap profile brings some complexity to the deposition process, as well as the characterization of the device. Therefore, the use of ungraded (flat bandgap) absorbers can provide better understanding of the limiting factors of the device, and accelerate solving some of the problems (Ochoa et al., 2020). Another way to counteract the low Voc is the implementation of a passivation layer at the interface to reduce recombination. Over the years, this concept has been getting more attention. For the rear surface, various dielectric materials (as passivation layer) and methods for the creation of contact openings have been implemented, and these reported studies have proven that passivation layers with contact openings can be used to reduce interface recombination (Birant et al., 2020a, 2020b, 2019; de Wild et al., 2021; Lopes et al., 2021; Vermang et al., 2014). In addition, studies have shown the combination of the aforementioned concept and post deposition treatment (PDT). One of these studies has shown that when an AlO_x passivation layer with contact openings is combined with potassium fluoride (KF) PDT on graded CIGS, the performance of the device increases (Lopes et al., 2021). Another study has highlighted that when an AlO_x passivation layer with contact openings is combined with rubidium fluoride (RbF) PDT on ungraded CIGS, the performance of the device decreases (de Wild et al., 2021). These two studies point at the fact that similar attempts can give different results depending on which CIGS absorber or alkali is used. Hence, the combination of PDT and passivation needs to be carefully studied. The application of a passivation layer with contact openings is mainly used for the rear surface of CIGS. For the front surface, on the other hand, this concept is still immature due to some challenges. Firstly, the pattern creation for the contact openings on the front surface is more challenging than the rear surface due to the roughness of the absorber. Secondly, the selected passivation material has to be compatible with further processing. Alternatively, the production steps of the solar cells need to be adapted if the selected material is not compatible. This is often complex and requires time consuming process re-optimization. So far, only a few studies investigated the use of a thin passivation layer for the front interface of CIGS and kesterite (CZTS) and its impact on the device level (Garud et al., 2018; Park et al., 2018). It has been shown that when a GaO_x layer (<2nm) is implemented at the CIGS/CdS interface, the device performance increases by an absolute of 2.6% (Garud et al., 2018). In another study, a thin AlO_x layer (<5nm) was applied at the CZTS/CdS interface, and the device performance increased. Moreover, it has been shown in that work, that even if AlO_x is etched by ammonium-hydroxide during the CdS deposition, the CZTS surface is passivated by hydrogen during the atomic layer deposition (ALD), and thus the performance of the device improves compared to the reference (Park et al., 2018). Löckinger et al. have shown that by using a NaCl template pattern, contact openings can be created in a 10nm thick HfO_x layer. This layer can then be implemented into the solar cell structure without changing the conventional chemical bath deposition (CBD) due to the chemical inertness of the HfO_x (Löckinger et al., 2019). In another study, a SiO_2 nanosphere template was used to create contact openings in the AlO_x layer (5.5nm) and the solar cell was finished with ZnO/Al:ZnO (Hultqvist et al., 2017). Both reported studies did not show any improvement on the device level, as the performance of the devices were either lower than or comparable with the reference devices. Generally, AlOx has been seen as a promising candidate as passivation layer for front surface applications due to its lower density of interface defect (Dit) (Curado et al., 2020; Scaffidi et al., 2021). In our previous work, we showed that AlO_x exhibits lower Dit than HfO_x (Scaffidi et al., 2021), which was still true even when a combination of both materials was used in a AlO_x/HfO_x multi-stack design. We even suggested that the AlO_x/HfO_x multi-stack design is resistant to the conventional CBD of CdS. Furthermore, we showed that the contact openings can be created in an AlO_x/HfO_x multi-stack design by using NaCl pattern (Buldu et al., 2021). However, as the NaCl was deposited on the CIGS layer, some interaction between the NaCl template and the CIGS absorber occurred and led to a negative impact on carrier collection (Buldu et al., 2022). In

light of this information, in this work, we suggest using an alternative approach to create contact openings in oxide layers at the front interface. By using the alternative approach, it is not only possible to use any oxide layer, even if it would normally degrade during a conventional CBD process, but also to use any alkali salt available to create the template pattern, without risking adverse effects on the CIGS absorber layer. In the case of NaCl as a patterning alkali, these adverse effects could come from an excess concentration of Na in the CIGS absorber, which has been shown to be one of the reasons for poor device performance (Li et al., 2021; Puttnins et al., 2015). In addition, other alkali salts or nanopatterning materials, such as LiF or nanoparticles that is detrimental for the CCIGS absorber, could show promising results when it comes to patterning (Kandybka et al., 2021). Lastly, the interaction between the alkali template and the ones used for bulk treatment might lead to adverse effects on the solar cell performance (de Wild et al., 2021). Thus, it is of overall interest to have access to an approach that allows for the deposition of oxide layers with contact openings at the front interface of CIGS, while preventing the diffusion of the materials used for the creation of said pattern into the CIGS absorber layer.

2.Experimental Method

The CIGS layer was deposited on a SLG/Si(O,N)/Mo substrate by using a one-stage co-evaporation method. A Si(O,N) alkali diffusion barrier is used to prevent any alkali diffusion from the SLG. During the CIGS deposition, the evaporation rate of all sources was kept constant until the desired thickness was reached. The final thickness of the absorber layer is 1.6µm. With the help of this process, an ungraded CIGS absorber with a Cu/(Ga+In) ratio of 0.77-0.82 and Ga/(Ga+In) ratio of 0.3 was produced. The composition was measured with X-ray fluorescence. Before any other process was applied on samples, the CIGS surface was treated with ammonium sulfide $((NH_4)_2S)$ as described in our previous work (Buldu et al., 2020).

KF post deposition treatment (PDT): 0.2M KF was spin-coated on samples that are mentioned in section 3.3. Then samples were annealed at 350 ^{o}C for 15 minutes under N_2 atmosphere. During the annealing, samples were covered with a Mo/Si(O,N)/SLG substate. The details can be found in a pre-existing work (De Wild et al., 2019). After the application of KF-PDT, samples were cleaned with a 10% HCl solution for 30 seconds to remove surplus KF from the CIGS surface. In addition, by doing this, we avoided altering our NaCl patterning as much as possible.

Patterning: A NaCl solution is used to create the pattern for the contact openings (Löckinger et al., 2019). This surface patterning is based on self-assembly processes (Reinhard et al., 2015). A 0.5M NaCl solution was preheated at 50 ^{o}C after which the samples were dipped into the solution for 90 seconds, for more details see (Buldu et al., 2022, 2021). The roughness of the substrate plays a key role when it comes to the self-assembling of NaCl islands. The effect of the surface roughness on the patterning can be seen in Supporting Fig.1. When a smooth surface like molybdenum was used, the formed pattern is more compact and better arranged as compared to the CIGS surface. In addition, the roughness of the CIGS surface can be affected by the chosen deposition technique, or the thickness of the absorber (De Wild et al., 2020; Mollica, 2017). The roughness of CIGS increases from 40nm to 148nm when the thickness of the absorber layer is increased from 500nm to 1600nm. The change of the CIGS roughness has a significant impact on the formed pattern on the surface, the NaCl islands showed a more compact pattern on the surface of thin CIGS (like molybdenum) than that of the thicker CIGS.

Multi-stack oxide layer: Both AlO$_x$ and HfO$_x$ layers were deposited via atomic layer deposition (ALD) at 150 ^{o}C and 250 ^{o}C, respectively. The HfO$_x$ layer was deposited on the AlO$_x$ layer to protect it during the buffer layer deposition. 8nm AlO$_x$ was deposited with a growth rate of

0.17nm/cycle. Trimethylaluminium (TMA) and H_2O were used as precursor and reactant, respectively. 2nm HfO_x layer was deposited with a growth rate of 0.14nm/cycle. Tetrakis-EthylMethylAmino Hafnium (TEMAH) was used as precursor and H_2O as reactant.

HCl cleaning: This step was only applied on AlO_x to change the surface properties. Our as-deposited AlO_x layer surface is hydrophobic and NaCl salts do not form on this surface. To create the NaCl salt pattern, CIGS/AlO_x samples were dipped in 10% HCl solution for 2 minutes at room temperature. After that, samples were dipped in an NaCl solution immediately. Before the CdS layer deposition, the samples with multi-stack oxide layer design were dipped into the ultrasonic water bath to remove the salts and create the holes in the multi-stack oxide layers, or the HfO_x layer depending on the approach. After these steps, the solar cells were prepared. A CdS buffer layer was deposited at 65 °C. 2.7 mM cadmium acetate dihydrate, 95mM thiourea and 2M ammonium hydroxide were used and the deposition took around 12-13 minutes. Lastly, samples were finished with 60nm i-ZnO/ 300nm Al:ZnO and Ni/Ag/Ni metal contacts. Samples are 2.5x5 cm^2, and cells of 0.5 cm^2 are mechanically scribed.

The time-resolved photoluminescence (TRPL) measurement was performed with a Picoquant FluoTime 300 system with a 532 nm excitation wavelength, time resolution of 25ps and a repetition rate of 3MHz. The TRPL measurement was done on the samples for all the steps from bare (as-deposited) CIGS to window layer deposition. Scanning electron microscopy (SEM) imaging and energy-dispersive X-ray spectroscopy (EDS) analysis was done with a Tescan and Bruker SEM. The NaCl salts pattern formation on the sample surface and the creation of the contact openings was visualized with SEM. EDS was used to determine the composition in the openings and to ensure the presence of the multi-stack oxide layer after the buffer layer deposition. To be as surface sensitive as possible while guaranteeing accurate EDS measurements, they were performed at 10kV using a 12 beam intensity and a 150nm spot size and these parameters were remained constant for each measurement. The performance of the solar cells was measured with a Keithley 2400 source meter with four terminals under A.M 1.5 illumination at room temperature. For each sample, ten cells were measured. External quantum efficiency measurement (EQE) was performed under dark condition and measured from 350 to 1300nm with 10nm steps. Capacitance-Voltage (C-V) measurements were acquired with an Agilent E4980A Precision LCR meter. The solar cells were measured at room temperature and DC bias range was varied from -2.5V to 1V with 0.1V steps. For each sample, an apparent doping profile was extracted at 100kHz to prevent signal contribution from defect charge carrier states as much as possible. (Puttnins et al., 2013)

3. Result and Discussion

3.1. Creation of point openings in the multi-stack oxide layer

A NaCl salt solution is used to create a pattern for contact openings in the oxide stacks. Depending on the placement of the NaCl in the multi-stack oxide layer, the direction of contact opening creation changes. Therefore, depending on the direction, this approach is called bottom-up (BU) or top-down (TD).

3.1.1. Bottom-Up (BU) Approach

In the BU approach, an NaCl salt pattern is created on the CIGS surface followed by the oxide layer deposition. The holes in the oxide stack then form at the positions of the salt crystals after the ultrasonic water bath. The design steps from beginning to end of solar cell production is shown in Fig. 1. More details can be found in our previous work (Buldu et al., 2022).
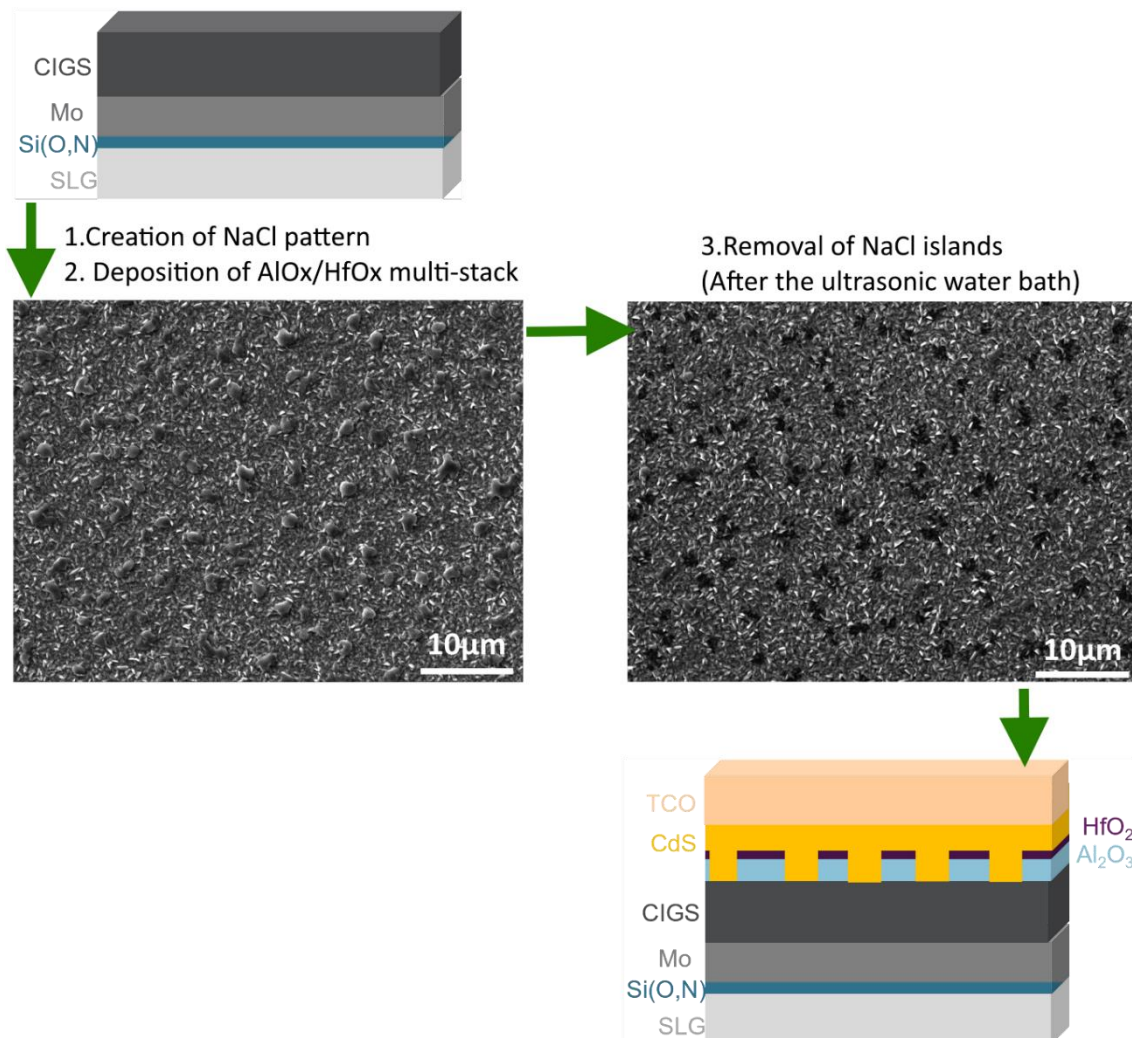
Fig. 1.Schematic representation of the steps for the application of the AlO_x/HfO_x multi-stack oxide layer with contact openings using the bottom-up approach.

An EDS measurement is performed after the second and third step to ensure that contacts are created fully before the buffer layer deposition. Table 1 shows the extracted atomic percentage of the elements from the EDS measurement, which revealed that the contact openings are successively created after the ultrasonic wash bath step. Moreover, this indicates that the AlO_x layer under the HfO_x is not etched during the buffer layer deposition.

Table 1
The average atomic percentage of the elements. For step numbering see Fig. 1.

Steps		Cu	Na	O	Al	Hf	Cd	S
1-2	Oxide stack	20.1	2.8	14.3	3.3	0.5	/	/
	Salt	6.5	41.7	7.9	1.4	0.3	/	/
3	Oxide stack	19.7	3.5	15.3	3.5	0.5	/	/
	Hole	24.7	0.5	2.5	0.5	0.1	/	/
After CdS	Oxide Stack	22.4	0.6	7.4	1.9	0.4	0.9	1.1
	Hole	20.9	0.2	1.1	/	/	6.3	5.9

3.1.2. Top-Down (TD) Approach

In the TD approach, a NaCl salt pattern is created on top of the AlO_x layer. By doing this, any contact between NaCl template and CIGS is prevented. Initially, the AlO_x layer was deposited onto the CIGS surface. Then, an NaCl salt pattern was formed on the AlO_x, and as a last step, a HfO_x layer was deposited on this structure. With this approach, the contact openings are not

created in the same way as with the bottom-up approach, since when the NaCl salts dissolve during the ultrasonic water bath, they only create holes in the HfO$_x$ layer. The contact openings can be fully created using a mild ammonium hydroxide solution removing the AlO$_x$. In this work, the sample is dipped into the 5% ammonium hydroxide solution at room temperature prior to the buffer layer deposition. Fig. 2 is the schematic representation of the creation of the multi-stack oxide layer design contact openings using the top-down approach. The top SEM image (1-4 step) shows the multi-stack oxide layer with the NaCl pattern before the creation of openings. After the ultrasonic water bath wash (step 5), the NaCl salts were removed, leaving behind lighter areas highlighted with orange arrows on the bottom SEM image in Fig. 2. After the mild ammonium hydroxide etching (step 6), it can be clearly seen in the bottom right SEM image that the pattern fully appears. This is the first indication the multi-stack oxide layer with contact openings is successfully formed on the CIGS surface.
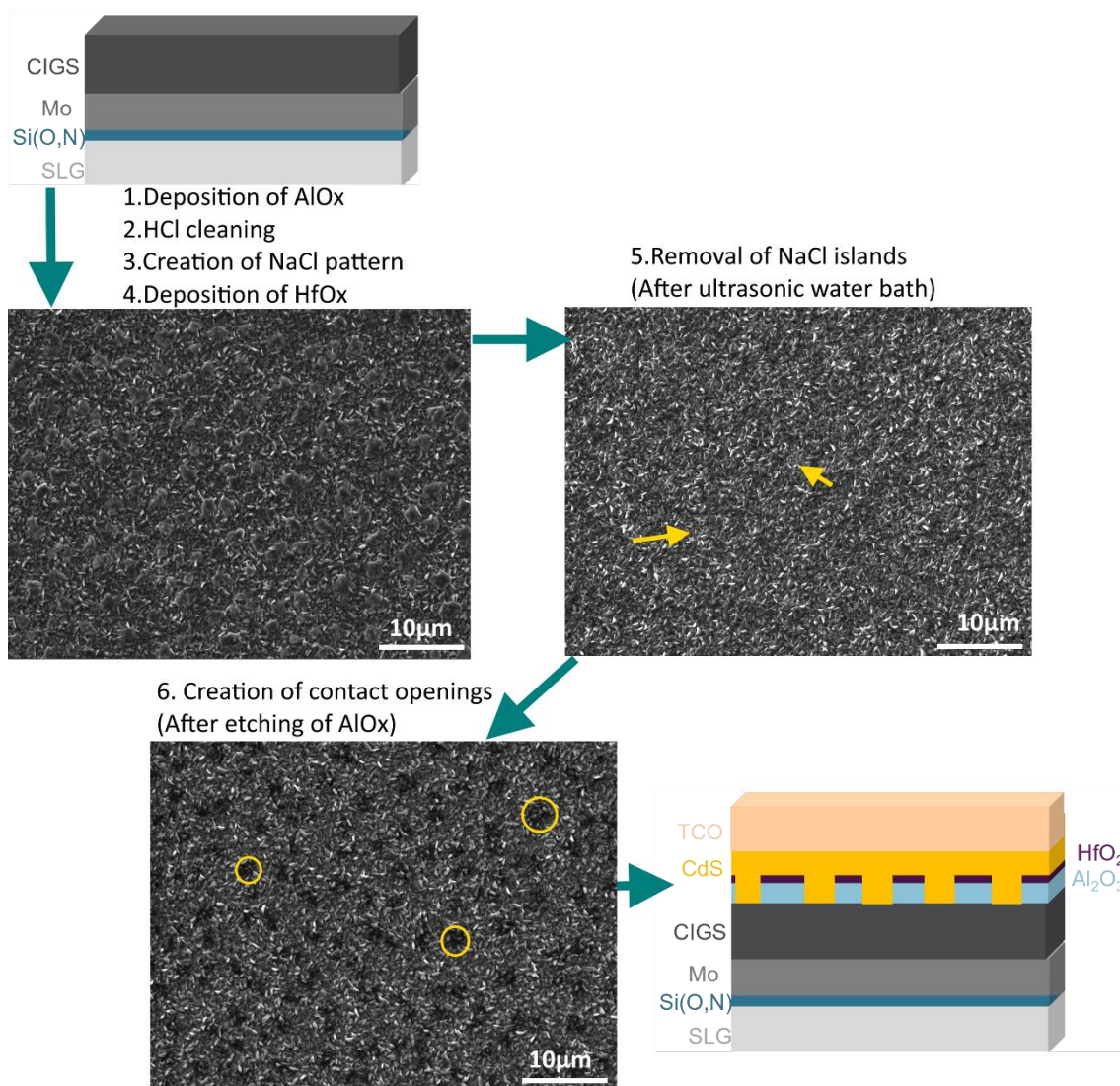

Fig. 2.Schematic representation of the steps for the application of the AlO$_x$/HfO$_x$ multi-stack oxide layer with contact openings using the top-down approach. The yellow arrows point at the lighter areas where the NaCl islands have left holes in the HfO$_x$ layer. The yellow circles highlight some of the fully formed contact openings in the multi-stack oxide layer after the etching of AlO$_x$.

EDS measurements are performed on the top-down samples at several points during the experiment. To ensure that the AlO$_x$ layer does not get damaged during the HCl etching, the first EDS measurement was done after the fourth step (see the top left SEM image on the Fig.

2). As can be seen in Table 2, the multi-stack oxide layer of the top-down approach was created on a CIGS surface successfully. After the ultrasonic wash (step 5), most of the NaCl salts are removed from the surface, (see Fig. 2), and a pattern is formed on the surface. The EDS measurement revealed that the lighter areas, shown with yellow arrows on the top right SEM image in Fig. 2, indicate where partial openings were created by removal of NaCl salts. To create fully open contacts, a mild ammonium hydroxide solution was used to etch the AlO_x, since it is not chemically resistant to ammonia-based solutions (Li et al., 2014). After this etching step (step 6), the EDS measurement was performed on the areas which are shown with yellow circles in Fig. 2. These areas do not contain Al, Hf or O elements, hence it can be said that holes were successfully created in the multi-oxide layer. The last measurement is done after the buffer layer deposition to ensure that the CdS/multi-stack oxide (AlO_x/HfO_x)/CIGS is created without any damage while creating the CdS/CIGS contact through the holes. As can be seen on Table 2, the multi-stack oxide layer with contact openings is successfully implemented at the CdS/CIGS interface.

Table 2
The average atomic percentage of the elements. For step numbering see Fig. 2.

Steps		Cu	Na	O	Al	Hf	Cd	S
1-4	Oxide stack	21.9	0.6	11.4	3.1	0.6	/	/
	Salt	10.9	31.2	7.8	2.1	/	/	/
5	Dark	21.7	0.3	9.6	2.9	0.6	/	/
	Light	22.1	0.6	10.1	2.5	0.2	/	/
6	Oxide Stack	21.5	0.4	11.1	2.8	0.6	/	/
	Hole	25.3	0.2	0.3	/	/	/	/
After CdS	Oxide stack	21.8	0.6	10.8	3.1	0.6	0.5	0.5
	Hole	20.2	0.2	5.8	/	/	6.7	6.5

3.1.3. Comparison of the creation of the contact openings on different surfaces
An NaCl pattern was created on different surfaces with both approaches introduced above. Surface properties (such as roughness) can affect the pattern formation, the effect of the roughness on the formation of the pattern can be seen in Supporting Fig.1. Nevertheless, in this case, we observed no significant difference in the formation of the pattern when both approaches are compared. As can be seen in Fig. 3, the width of contact openings is around 1µm, and the distance between two openings (pitch) shows fluctuations from 1µm to 8µm due to random patterning. However, 76.4% of the pitch sizes are lower than 3µm in the TD approach, and 46% in the BU approach. Thus, the top-down approach has slightly more compact contact openings than the bottom-up approach. Given the impact of the surface roughness on the pattern formation (Supporting Fig. 1), this could also be due to a slight difference of the roughness between the two absorber layers. Since the roughness of the CIGS is higher than the thickness of the AlO_x layer we deposit, it's presence should have only a negligible impact on the overall roughness of the sample.
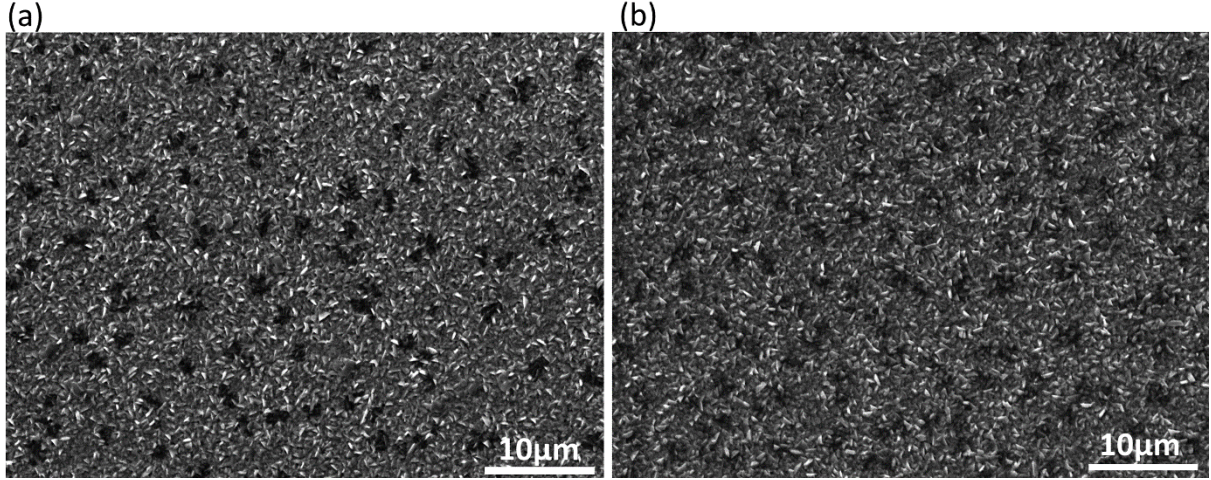
Fig. 3. SE micrograph of the multi-stack oxide layer with contact openings on the CIGS surface. Contact openings were created using (a) the bottom-up approach and (b) the top-down approach.

3.2. Comparing the impact of the implementation of a multi-stack oxide layer into the CIGS architecture using the bottom-up and top-down approaches

To study the impact of both the BU and TD approaches on the material characteristics and performance of our solar cells, two series were produced. To include the effect of the NaCl pattern on the CIGS absorber, both series have their own reference. The reference of the TD series (REF-TD) is a standard CIGS solar cell as produced following our in-house baseline process, but without Na. The reference of the BU series (REF-BU) underwent the NaCl pattern deposition on the CIGS layer, which was then followed by a 150°C-1h anneal to mimic the expected Na diffusion into the absorber layer during the ALD deposition. TRPL measurements were performed from bare CIGS layer up to the window layer deposition since it is an effective tool to gather information about the bulk properties of CIGS and its surface quality. The change in the PL decay time is represented in Fig. 4. Looking at the PL decay curves, we can say that the PL decay time is improved after the implementation of a multi-stack oxide layer regardless of the approach. However, the PL decay time was decreased after the CdS buffer layer deposition. In addition, the PL decay time reduction in the BU approach was slightly more severe than for the TD approach. To extract decay lifetime information from the measurements, the PL decay time curves were fitted with a bi-exponential function.

$$I_{PL}(t) = A_1 e^{-t/\tau 1} + A_2 e^{-t/\tau 2} \qquad (1)$$

where A_1 and A_2 are coefficients, and τ_1 and τ_2 is the fast and slow decay lifetime, respectively. It has been reported that the fast decay (τ_1) is associated to the interface recombination or charge separation, and the slow decay (τ_2) is linked to bulk recombination(Curado et al., 2020; Heise and López Salas, 2017; Shimakawa et al., 2008). Table 3. gives the summary of the obtained TRPL data for all curves in Fig. 4.

Table 3
Summary of the data obtained from the TRPL curve by fitting biexponential function.

Sample		τ_1	τ_2	$\tau_{average}$ $\dfrac{A_1\tau_1{}^2 + A_2\tau_2{}^2}{A_1\tau_1 + A_2\tau_2}$
BU-approach	Bare CIGS	0.93	2.94	0.98
	CIGS/Multi-stack	1.18	3.64	1.4
	After CdS	0.99	3.05	1.1

REF-BU	After CdS	0.91	2.64	0.96
TD-Approach	Bare CIGS	0.93	2.87	0.99
	CIGS/Multi-stack	1.31	4.18	1.69
	After CdS	1.18	3.73	1.45
REF-TD	After CdS	1.05	3.08	1.14

As can be seen in Table 3. our samples have a low PL decay time from the beginning. Nevertheless, both fast and slow decay improved after the implementation of the multi-stack oxide layer. However, the improvement in lifetime for the TD approach was slightly higher than the BU approach. Even though their bare CIGS PL decay time were similar to each other, the improvement in the PL decay time after the addition of multi-stack oxide layer was different. This difference points to the fact that when the NaCl pattern is formed on the CIGS (in case of the BU approach), it may lead a negative impact. Furthermore, after the CdS deposition, both τ_1 and τ_2 of the BU and TD approach were decreased, hence it seems like the CdS and oxide layer has a competing effect. As mentioned earlier τ_1 can be linked to the charger separation (Heise and López Salas, 2017). Hence, based on our results, we can conclude that the charge separation in both the CdS (reference samples) and multi-stack oxide layer (before the CdS deposition) case is similar. This hints at the fact that the electric fields created by CdS and the multi-stack oxide layer have a similar ability to separate the charge carriers. However, the decrease in PL decay time in the multi-stack samples after the CdS deposition indicates that the overall electric field created by the combination of both layers is of a lower intensity. This, it is reasonable to assume that the electric fields created by the multi-stack oxide layer and the CdS are opposite in direction. Despite this the remaining lifetimes of the multi-stack samples were still higher than of their references. It should also be noted that the PL decay time of the REF-BU is lower than the REF-TD, once again this hints at the fact that NaCl may have a negative impact on the absorber, since the main difference is that the REF-BU sample has NaCl pattern on it. According to these results, it can be said that the implementation of the multi-stack oxide layer may help to reduce recombination and subsequently increase the PL decay time. However, the addition of the CdS layer on multi-stack design suppresses this positive impact of the multi-stack due to their competing effects.
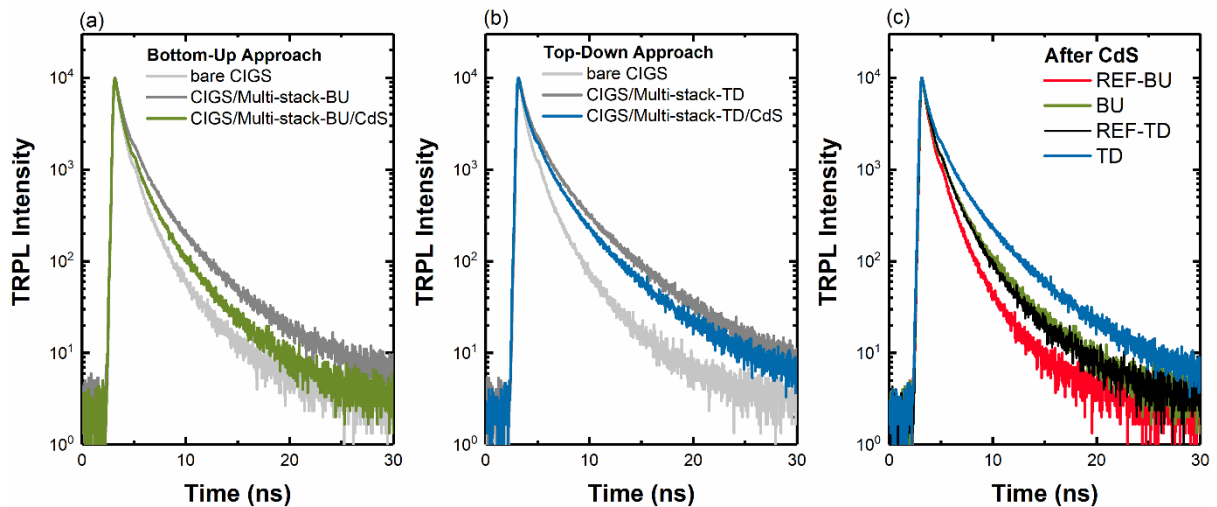

Fig. 4. The PL decay time evolution from bare CIGS to CdS deposition. (a) The PL decay time increases when the multi-stack oxide layer is applied with the BU approach (dark grey solid line), then decreases after CdS deposition (green solid line). (b) The PL decay time increases when the multi-stack oxide layer is applied with the TD approach (dark grey solid line), then decreases slightly after CdS deposition (blue solid line). (c) The PL decay time comparison after CdS deposition for all samples.

Lastly, solar cells were produced from each sample to investigate the effect of the bottom-up and top-down approaches on the solar cell performance. At first glance, we noticed some unexpected performance differences between REF-BU and REF-TD. Generally, a higher PL decay time should result in a higher Voc (Ohnesorge et al., 1998; Shimakawa et al., 2006; Shirakata and Nakada, 2007). Here, even though the PL decay time of REF-BU is slightly lower than the one of REF-TD, the resulting solar cell shows a higher Voc. This difference could be due to a higher doping in the REF-BU sample stemming from the additional Na supply from the pattern. This option will be discussed further in a later part of this paper. Furthermore, another interesting observation is that even though the BU approach shows a higher PL decay time than its reference, the Voc is lower in this sample. On the other hand, the TD approach shows higher Voc than its reference and the improved PL decay can be one of the reasons for this.

Unfortunately, the performance of the devices decreases with the addition of the multi-stack design (Table 4.). Even though the Voc improves slightly with the TD approach, the FF and Jsc decreases while, and in the case of the BU approach all JV parameters decrease. Consequently, we believe that the reason for the poor device performance for both approaches is mostly due to current loss and low FF. The JV curves were investigated to gain more insight on the device characteristic. Looking at the JV curves in Fig. 5(a), it is apparent that some solar cells suffer from a medium to pronounced roll-over distortion. Most prominently, this can be observed for the REF-TD and TD, and for the REF-BU and BU to a smaller degree. This behavior can be explained by the presence of a barrier between absorber and back contact (Scheer and Schock, 2011). It has been reported that the absence of alkali elements in the absorber layer generally leads to a roll-over distortion in their JV curves which disappears with alkali addition (Czudek et al., 2020; Eslam et al., 2021; Li et al., 2021). Thus, in the case of the reference samples, the low Voc can be explained to some degree by the existence of the roll-over distortion. However, the same statement cannot be valid for the BU and TD device since the Voc of the BU device is lower even though the roll-over distortion is not present in its JV curve. Besides the roll-over distortion, it was also reported that the JV parameters, i.e Voc and FF, are strongly affected by the size of contact openings and their distribution, respectively (Sozzi et al., 2017). This means that a slight difference in contact openings could be an explanation for the lower Voc in the BU. At this point, it can be highlighted that the AlO_x in the TD device seems to act as a blocking layer for the Na diffusion from the NaCl pattern into the CIGS since its JV curve is still affected by the roll-over distortion. By further examining the JV curves of the BU and TD device, it can be seen that the photocurrent is voltage dependent. The photo current increases with reverse bias and decreases with forward bias, but no shunting was observed on the dark curve (solid lines in Fig.5a) This reduction of the current in the forward bias can be one of the reasons for the low FF, apart from the sub-optimal contact openings. However, at this point, the reason for the dramatic loss in Jsc is still open question. To understand the reason for the low current collection, EQE measurements were performed on these samples.

Table 4
The average solar cell parameters of the BU and TD approach and their references. The average was calculated from 10 randomly selected cells. (Supporting Fig.2)

Sample Name	Jsc (mA/cm^2)	Voc (mV)	FF (%)	Efficiency (%)
REF-BU	26.9±1.9	532±5	56.5±1.1	8.1±0.6
BU	13.6±2.6	508±4	43.1±2.1	2.9±0.7
REF-TD	27.3±1.1	506±1	55±0.6	7.6±0.3
TD	14.6±1.3	517±8	46.5±2.1	3.5±0.2

As can be seen in the EQE spectrum (Fig. 5 (b)), both the BU and TD approaches show low current collection in all wavelength regions. This overall deteriorated current collection could be due to a barrier for the photocurrent, which can be one of the reasons of the voltage dependence of photocurrent (Scheer and Schock, 2011). Furthermore, the TD approach, in particular, shows more severe problems than the BU approach. For the BU device, the measured Jsc for the J-V measurement (15.29mA/cm^2) was found to almost match the one Jsc calculated from EQE (16.64mA/cm^2). However, the measured and calculated Jsc showed significant difference in the case of the TD device, i.e. the measured Jsc is 16.26 mA/cm^2 and 10.29 mA/cm^2 for the Jsc calculated from EQE. Such a high difference can be the sign of either a higher barrier for the photocurrent and/or an effect related with absorber layer. We believe that if the multi-stack oxide layer is the reason for the barrier, its effects on the EQE spectrum should be similar in both devices. The deposition parameters of the multi-stack oxide layer are the same in both cases. The main difference is the existence of the Na on the CIGS during the deposition in the case of BU approach. which leads to additional diffusion of Na into the CIGS bulk. Since Na is known to passivate defects in CIGS, for example at the grain boundaries, this additional diffusion of Na could result in a better overall absorber quality (Cojocaru-Mirédin et al., 2021). We then speculate that, in the absence of Na diffusion, i.e. in the case of the TD device, electrons have a higher probability to recombine which leads to a lower carrier collection. Alternatively, it could be possible that the electric field created by multi-stack oxide is stronger, i.e electrons are more heavily repelled from the front interface, which would lead to a similar result. These phenomena might then be worsened by the absence of illumination (or bias) in the case of the EQE measurement.

To exclude changes in optical bandgap as the reason for the observed deteriorated carrier collection in the long wavelength region, the optical bandgap was determined from EQE measurement by using the (E x EQE)^2 method (Carron et al., 2019) (Supporting Fig. 3). It was found that the optical bandgap does not vary between the devices with oxide layers and their respective references. Thus, a variation in bandgap can be safely discarded as the reason of the deteriorated carrier collection. Another possible explanation for the collection losses at long wavelength could be differences in the space charge region width (W_{dep}). To investigate this, C-V measurements were performed on these devices. The apparent doping (N_{cv}) and the W_{dep} were calculated using the Mott-Schottky relation,

$$N_{cv} = \frac{2}{\varepsilon q A^2} \left[\frac{d(\frac{1}{C^2})}{dV} \right]^{-1} \quad \text{and} \quad C = \frac{\varepsilon A}{W_{dep}} \tag{2}$$

where C is the measured capacitance, A is the effective area of the solar cell, and ε is the permittivity of CIGS. The apparent doping profile for each sample is given in Fig. 5(c). The N_{cv} were estimated from the minimum of the curve, and the empty square and circle on the curves indicates the W_{dep} at 0 V dc bias. The N_{cv} and W_{dep} values for each sample are summarized in Table 5.

Table 5. The Ncv and Wdep values for the BU and TD approach and their reference samples.

Sample Name	Apparent doping N_{cv}(cm^{-3})	Space charge region width W_{dep} (μm) (at 0V)
REF-BU	5.5 x10^{14}	0.36
BU	10.5 x10^{14}	0.19
REF-TD	5.8 x10^{14}	0.73
TD	7.2 x10^{14}	0.17

At first glance, it can be seen that the apparent doping profile of the BU and TD approach do not show significant difference to their references. All samples showed a U-shaped apparent doping profile, which is a typical characteristic in CIGS solar cells (Werner et al., 2018).

However, the addition of Na (in case of the BU approach and REF-BU) caused a slight difference in the apparent doping profile as compared to the absence of Na. The apparent doping of the BU approach and its reference sample increases towards the front interface this probably comes from Na diffusion into the absorber. Neither the BU nor the TD approach cause significant change in the apparent doping, see dotted line in Fig. 5(c), but even small change in the apparent doping can have impact on the Voc. From the calculations, the increased in Voc was estimated to be 6mV for the TD sample (Pianezzi et al., 2014). From the JV measurement, the observed improvement in Voc was 11mV. This indicates that both increase in the doping level and improved PL decay time have impact on the increase in Voc. However, the Voc of the BU sample was lower than its reference even though its doping level and PL decay time was high. This hints that there is an additional, unexpected, problem requiring further investigation. Besides, the W_{dep} changes significantly with the addition of the multi-stack design. These results are different than the generally observed trend on the other studies, since the doping and space charge region width has a close relation, i.e higher doping causes a decrease in W_{dep} (Andres et al., 2018; Eslam et al., 2021). We think that the decreased W_{dep} in the BU and the TD approach could be due to the charge of the multi-stack oxide layer. Furthermore, these results indicate that the observed current loss for both approaches does not only come from the change in the W_{dep} due to the higher doping, since the observed change in doping is rather negligible. Neither does the change in the W_{dep} fully explain the current loss, especially in the short wavelength region. Therefore, we believe that this pronounced current loss could be caused by our multi-stack oxide layer, since our multi-stack design has a negative charge density (Scaffidi et al., 2021). Due to this, the electrons are repelled at the interface, resulting in reduced recombination, and potentially hindering the current collection.
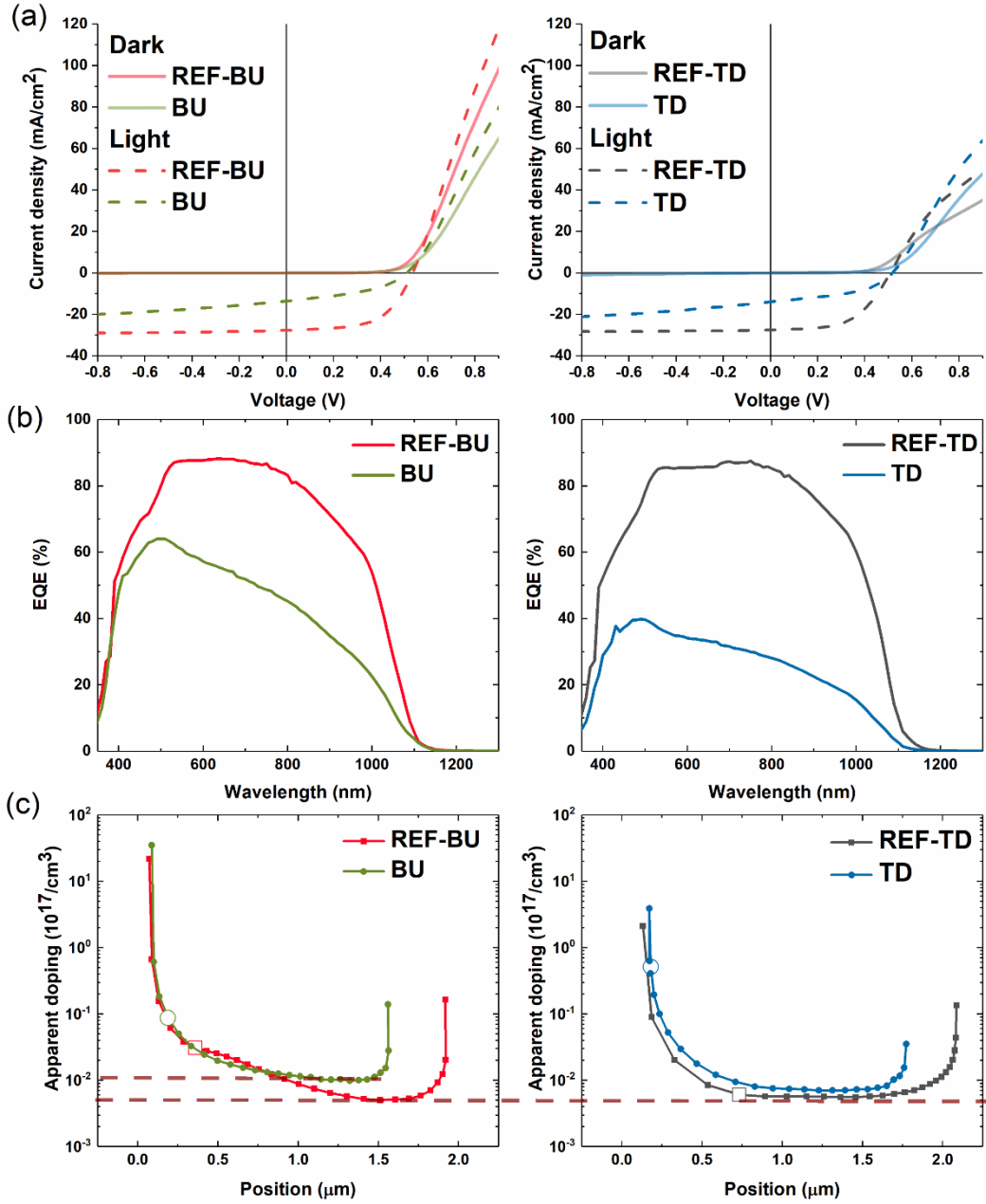
Fig. 5. The results of the bottom-up approach and its reference are shown on the left side, for the top-down approach on the right side. (a) The comparison of the dark and light JV curves of the multi-stack samples with their references. (b) The EQE spectrum for each device. (c)The apparent doping profile was at 100kHz extracted from C-V measurement. The empty square and circle points on the curve correspond to the W_{dep} at 0V bias.

3.3. Combination of KF treatment and multi-stack design with bottom-up and top-down approach for front interface applications

So far, the used CIGS absorber in this work did not contain any alkali elements until preparation of the oxide layers. It is generally accepted that the absorber layer quality improves when an alkali element (such as Na) is present (Czudek et al., 2020; Pianezzi et al., 2014). This can also be seen when the REF-BU device is compared to the REF-TD device in section 3.2. In this section, we applied a KF post deposition treatment to improve the absorber quality. This alkali was specifically selected because, while the aim is to improve the absorber quality, it should always remain possible to distinguish the effect of the PDT from the effect of NaCl, since the BU approach intrinsically supplies Na to the absorber. Three samples were used in this section, the first of which was used as a reference, and is named KF-REF, and neither of the approaches

was applied on this sample. The other two samples were produced with the bottom-up and top-down approaches, and are named as KF-BU and KF-TD, respectively. Initially, a TRPL measurement was performed for each step. The PL decay time curves were fitted by using Eq.1, and the summary of the fit values were given in Table 5. The beneficial impact of the KF PDT can be seen when the PL decay time of the bare CIGS (in section 3.2) and KF-treated CIGS are compared. The PL decay time of KF-treated sample is higher.

Table 6.
Summary of the data obtained from TRPL curve by fitting biexponential function.

Sample		τ_1	τ_2	$\tau_{average}$ $$\frac{A_1\tau_1{}^2 + A_2\tau_2{}^2}{A_1\tau_1 + A_2\tau_2}$$
BU-approach	KF treated-CIGS	1.01	3.62	1.20
	CIGS/Multi-stack	2.35	7.85	4.73
	After CdS	1.37	5.09	2.03
TD-Approach	KF treated-CIGS	1.01	3.57	1.23
	CIGS/Multi-stack	2.44	8.17	4.91
	After CdS	1.65	6.44	3.15
KF-REF	After CdS	2.81	9.18	5.52

When the multi-stack oxide layer was applied to the CIGS surface (KF treated CIGS cleaned with HCl), the PL decay time was significantly improved regardless of the approach (see Fig. 6 a and b). The PL decay time of the KF-REF sample was increased after the buffer layer deposition, and its PL decay time was higher than the REF-BU and REF-TD. It can be said that the KF treatment on the CIGS has a more significant impact on improving the lifetime than the NaCl (in the case of REF-BU). Furthermore, as mentioned in the previous section, the electric fields created by CdS and multi-stack oxide layer have similar impact on the charge carrier separation, since the short decay time values were similar in both cases. When the CdS layer was deposited on the KF-BU and KF-TD samples, the PL decay time decreased, and this behavior was expected since we made a similar observation for both the BU and TD samples in section 3.2. In this case, the decrease in the PL decay time of the KF-BU sample was more severe. The TD approach, on the contrary, showed a much more minimal decrease after the buffer layer deposition. These results indicate that when the pattern template is formed on the CIGS surface, i.e. in case of BU approach, a detrimental interaction between the bulk treatment (in this case KF PDT) and the interface application occurs. Hence, in the case where PDT treatment is applied to the bulk, the TD approach seems more favorable. Furthermore, in contrast with what is observed in the previous section, both the PL decay time for both the KF-BU and KF-TD samples was lower than that of KF-REF after the CdS deposition.
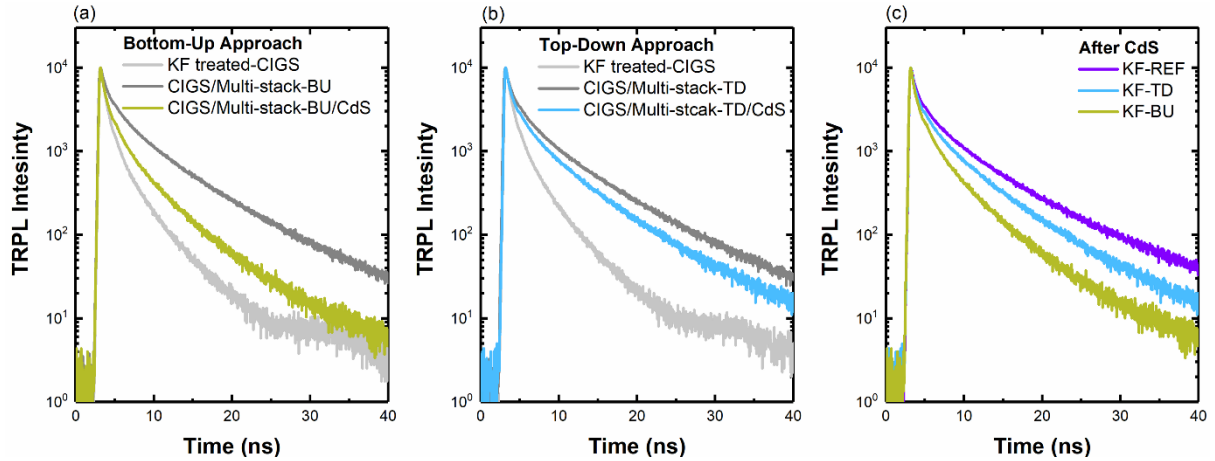
Fig. 6.The PL decay time evolution from KF treated- CIGS to CdS deposition. (a) The PL decay time increases when multi-stack oxide layer is applied with the BU approach (dark grey solid line), then decreases after CdS deposition (green solid line). (b) The PL decay time increases when multi-stack oxide layer is applied with the TD approach (dark grey solid line), then decreases slightly after CdS deposition (blue solid line). (c) The PL decay time comparison after CdS deposition for all samples.

Finally, solar cells were produced for each case. The roll-over distortion observed in the previous section disappeared after the KF treatment, see Fig. 7(a). Even though the KF-BU and KF-TD samples show better performances than the BU and TD samples (section 3.2), their device performances are lower than that of the KF-REF sample. The average solar cell parameters are given in Table 7. It clearly shows that all JV parameters deteriorate in the case of the KF-BU sample. Conversely, the Voc of the KF-TD sample remains at almost the same level as the KF-REF sample, but other parameters decrease. As mentioned earlier, a high PL decay time can lead a high Voc. In this section, it can be seen that the PL decay time of the KF-BU and KF-TD is lower than the KF-REF and the decrease in the Voc follows the trend of the PL decay time. Higher decrease in the PL decay time, higher drop in the Voc. The Jsc increases with KF treatment when the KF-BU and KF-TD are compared to the BU and the TD devices, but both KF-BU and KF-TD still suffer from a significant current loss in comparison to the KF-REF sample, similar to what was observed in section 3.2. In the previous section we avoid extracting the values for saturated current density (J_o), shunt and series resistance (R_{sh} and R_s) due to the presence of anomalies in the JV curves. However, in this section the JV curves did not show anomalies and the J_o, R_{sh} and R_s were extracted for each sample and summarized in Supporting Table 1. When the multi-stack design was implemented at the front interface, the R_s values increased from 0.5 Ohm.cm^2 to 1.1 Ohm.cm^2, regardless of the approach. This can be one of the reasons for the observed low FF. As we mentioned in the previous section, the geometry and size of the contact openings have significant impact on the solar cell parameters, and this indicates that even though the Rs does not significantly increase with the addition of the multi-stack design, the contacts size and their distribution still require an optimization (Sozzi et al., 2015). The R_{sh} increases with the multi-stack design from 9705 Ohm.cm^2 to 11165 Ohm.cm^2 (KF-BU) -11368 Ohm.cm^2 (KF-TD). J_o is an important parameter since it is related to the recombination in the solar cells. The J_o increased almost four times when the multi-stack design applied with the BU approach, whereas it decreased almost two times with the TD approach. The low Voc in the KF-BU can be explained by the increase in the J_o. This hints that although both the KF-BU and the KF-TD devices shows similar device performance, the recombination in the KF-BU device could be higher than in the KF-TD device. This observed behaviour could be also the same for the BU sample in the previous section. Since even though the BU sample showed slightly higher PL decay time than the REF-BU sample, the Voc was lower. If we assumed that the BU sample has slightly higher J_o than the REF-BU, which indicates higher recombination, then this could be another reason of the low Voc.

Table 7
The average solar cell parameters. The average was calculated from 10 randomly selected cells. (Supporting Fig.4)

Sample Name	Jsc (mA/cm^2)	Voc (mV)	FF (%)	Efficiency (%)
KF-REF	27.4±1.0	551±5	61.3±0.7	9.3±0.3
KF-BU	19.6±2.7	502±14	40.5±1.9	4.0±0.7
KF-TD	17.1±1.7	549±7	43.4±1.5	4.1±0.3

As can be observed in the EQE spectrum (Fig. 7(b)), the KF-BU sample shows a slight improvement in current collection, but a tremendous improvement is observed in the KF-TD sample after the KF treatment. The Jsc was estimated from EQE and compared to the measured Jsc, the estimated and measured Jsc is similar for all cases. In this section, the deposition of the multi-stack oxide layer is the same as in section 3.2, and the calculated optical bandgap from EQE (Supporting Fig.5) is similar to the one of the previous samples. Indeed, the only difference between both sections is the addition of the KF PDT. This leads to a better carrier collection in case of the multi-stack design resulting a in higher current. Therefore, it can be concluded that the TD sample in section 3.2 showed a dramatically deteriorated carrier collection due to worse bulk and/or interface quality, which is corrected by the application of a KF-PDT. In light of these results, we believe that the carrier collection is similar for both the BU and TD approaches when the absorber and/or interface quality is equalized. When comparing the CV results of both approaches, it appears that the apparent doping level remains similar to the KF-REF sample in the case of the TD approach, and slightly higher in the case of the BU approach (dotted line in Fig.7(c)). The shape of the apparent doping profile did not significantly change with the addition of the multi-stack design. Nevertheless, its addition caused a decrease in W_{dep}, similar to what was observed before. The N$_{cv}$ and W_{dep} values were summarized in Table 8.

Table 8.The N$_{cv}$ and W_{dep} values for the BU and TD approach and its reference sample.

Sample Name	Apparent doping N$_{cv}$(cm^{-3})	Space charge region width W_{dep} (µm) (at 0V)
KF-REF	2.5 x10^{15}	0.25
KF-BU	4.1 x10^{15}	0.09
KF-TD	2.6 x10^{15}	0.07

As can be seen, the apparent doping level is higher than in section 3.2. This can be an explanation for the high Voc in KF-REF compared to the REF-BU and REF-TD. However, when the multi-stack designs were compared, we observed that even though the N$_{cv}$ of the KF-BU is higher than the BU sample, the Voc is almost the same. On the other hand, in the case of the TD approach, the N$_{cv}$ of KF-TD is increased in the same way as for KF-REF when compared to the REF-TD and the TD samples. These results indicate that when the multi-stack design is used with the BU approach, it has a negative impact on the Voc, whereas the TD approach does not lead any negative impact on the Voc. In which case, this make the TD approach more suitable to create a contact opening when the alkali template is used.

In this work, the average device performance is low due to the fact that our samples do not have grading at the front/rear surface. This is expected to increase recombination at the rear/front surface and is one the reason for the poor device performance (Lafuente-Sampietro et al., 2021; Nakada, 2012). In addition, our samples contain small grains (<100nm), and therefore a large amount of grain boundaries which can act as recombination centers (Kohl et al., 2020). This is another plausible reason for the poor device performance. This possibility is highlighted by the fact that REF-BU and KF-REF showed higher performance than the REF-

TD, indicating that when the grain boundaries are passivated by alkali elements, the possible recombination at the grain boundaries is reduced resulting in better performance. The main purpose here was to tackle the front interface problem by implementing oxide layers to reduce the recombination at this surface. The two approaches represented here show that an oxide layer with contact openings can be implemented at the front interface. However, the device performances of the samples with oxide layers were lower than their reference samples. Nevertheless, the TD approach appeared to have more potential than the BU approach since it seems like recombination at the front interface can be reduced with the TD approach.
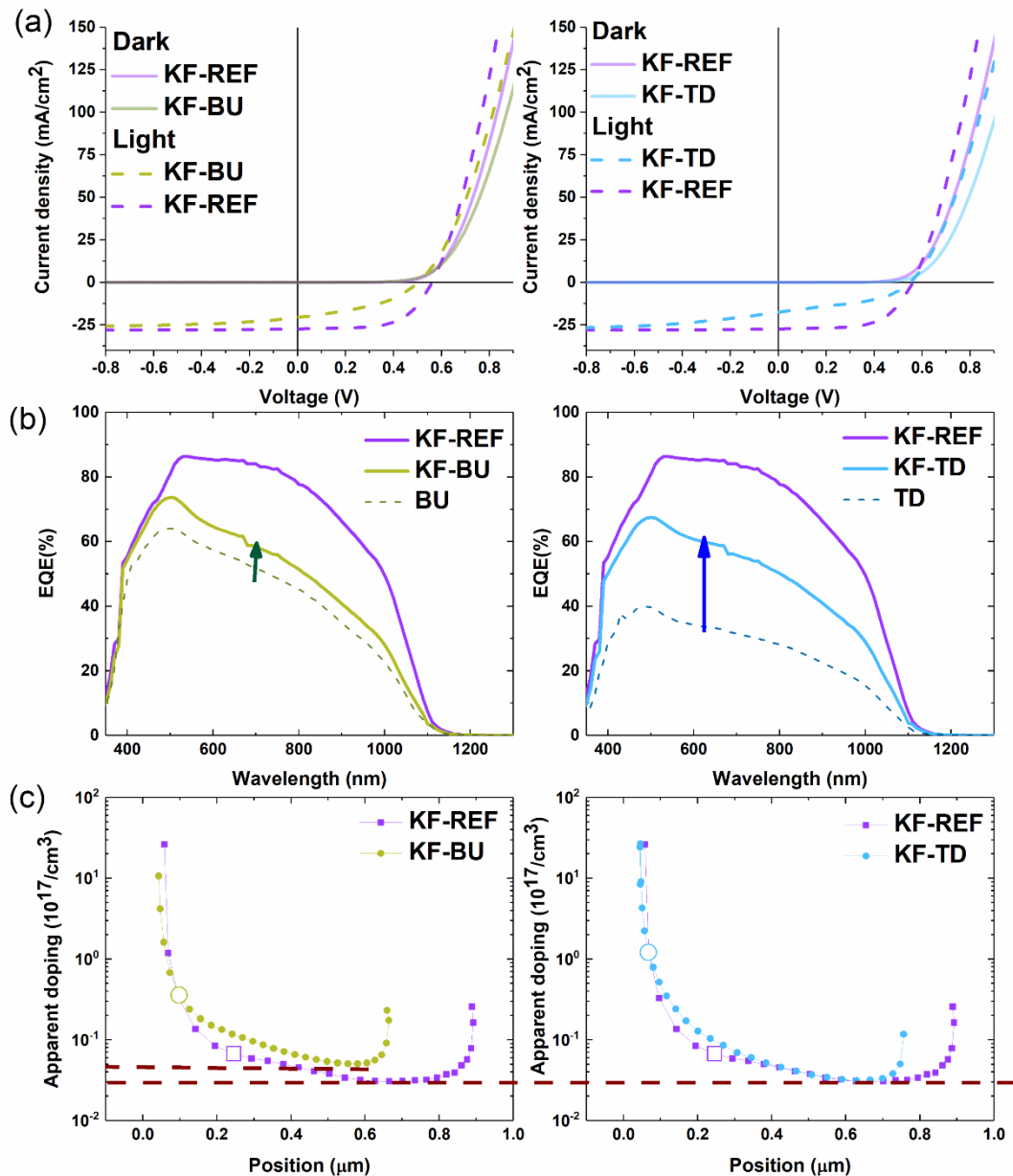

Fig. 7. The results of the bottom-up approach and its reference are shown on the left side, for the top-down approach on the right side. (a)The comparison of the JV curves for the multi-stack sample with KF-REF. (b) The EQE spectrum comparison for each device (dashed line the EQE response without KF treatment from section 3.2). (c) The apparent doping profile was at 100kHz extracted from C-V measurement. The empty square and circle points on the curve correspond to the W_{dep} at 0V bias.

4.Conclusion

In this work, we presented two approaches (bottom-up and top-down) to create contact openings using a multi-stack oxide layer design. We worked with an alkali-free as well as a KF treated CIGS absorbers to investigate the effect of the NaCl pattern template and the oxide layer. Analyzing TRPL measurements of both approaches, it appeared that the PL decay time increases significantly regardless of the approach. However, while PL decay time decreases after the CdS deposition for the TD approach, a more severe decrease was observed in the BU case. This indicates the potential existence of an unwanted negative effect of the NaCl pattern. The electrical characterization of our solar cells showed that in all cases, when the AlO$_x$/HfO$_x$ multi-stack with openings is applied at the CdS/CIGS interface, the device performance decreases dramatically. We observed that the main reason of this poor device performance is coming from Jsc loss and lower FF. We also observed that the Voc decreases (25mV) when the BU approach is used to create the contact openings. In the case of KF treated sample, the Voc is further decreased (50mV). Conversely, for the TD approach, the Voc remains constant or slightly increases regardless of presence or absence of bulk treatment. In absence of KF PDT, EQE and CV measurements showed that the BU approach has better carrier collection, probably due to Na diffusion into the bulk, resulting in better bulk properties and counteracting the apparent negative impact of the multi-stack oxide layer. However, for the KF-PDT samples, BU approach showed signs of detrimental interaction between the NaCl pattern and the KF treatment through the significant drop in Voc. The TD approach samples did not cause such a drop. This leads us to conclude that, the BU approach has an advantage over TD approach only in the case of untreated bulk absorbers, while overall, the TD approach shows promise in all situations. This might be because the TD approach prevents unwanted interactions with potential previous treatments to absorber or interfaces.

Considering all results obtained in this study, we would recommend the use of the top-down approach over the bottom-up alternative for the application of oxide layers to the front interface of the CIGS absorber. Further research needs to be focused on finding the right combination of materials to erase the detrimental impact of the oxides observed in the present study.

Acknowledgment

Reference

Andres, C., Schwarz, T., Haass, S.G., Weiss, T.P., Carron, R., Caballero, R., Figi, R., Schreiner, C., Bürki, M., Tiwari, A.N., Romanyuk, Y.E., 2018. Decoupling of optoelectronic properties from morphological changes in sodium treated kesterite thin film solar cells. Sol. Energy 175, 94–100. https://doi.org/10.1016/j.solener.2018.03.067

Birant, G., de Wild, J., Kohl, T., Buldu, D.G., Brammertz, G., Meuris, M., Poortmans, J., Vermang, B., 2020a. Innovative and industrially viable approach to fabricate AlOx rear passivated ultra-thin Cu(In, Ga)Se2 (CIGS) solar cells. Sol. Energy 207, 1002–1008. https://doi.org/10.1016/j.solener.2020.07.038

Birant, G., de Wild, J., Meuris, M., Poortmans, J., Vermang, B., 2019. Dielectric-based rear surface passivation approaches for Cu(In,Ga)Se 2 solar cells-A review. Appl. Sci. 9. https://doi.org/10.3390/app9040677

Birant, G., Mafalda, J., Scaffidi, R., De Wild, J., Buldu, D.G., Kohl, T., Brammertz, G., Meuris, M., Poortmans, J., Vermang, B., 2020b. Rear surface passivation of ultra-thin CIGS solar cells using atomic layer deposited HfOx. EPJ Photovoltaics 11, 1–5. https://doi.org/10.1051/epjpv/2020007

Buldu, D.G., De Wild, J., Kohl, T., Birant, G., Brammertz, G., Meuris, M., Poortmans, J., Vermang, B., 2022. A Novel Strategy for the Application of an Oxide Layer to the Front Interface of

Cu(In,Ga)Se2Thin Film Solar Cells: Al2O3/HfO2Multi-Stack Design with Contact Openings. IEEE J. Photovoltaics 12, 301–308. https://doi.org/10.1109/JPHOTOV.2021.3120515

Buldu, D.G., Wild, J. De, Kohl, T., Birant, G., Brammertz, G., Poortmans, J., Vermang, B., 2021. A multi-stack Al 2 O 3 / HfO 2 design with contact openings for front surface of Cu (In , Ga) Se 2 solar cells. 48th IEEE Photovolt. Spec. Conf.

Buldu, D.G., Wild, J. De, Kohl, T., Brammertz, G., Birant, G., Meuris, M., Poortmans, J., Vermang, B., 2020. Study of Ammonium Sul fi de Surface Treatment for Ultrathin Cu (In , Ga) Se 2 with Different Cu /(Ga þ In) Ratios. Phys. Status Solidi Appl. Mater. Sci. 2000307, 1–7. https://doi.org/10.1002/pssa.202000307

Carron, R., Andres, C., Avancini, E., Feurer, T., Nishiwaki, S., Pisoni, S., Fu, F., Lingg, M., Romanyuk, Y.E., Buecheler, S., Tiwari, A.N., 2019. Bandgap of thin film solar cell absorbers: A comparison of various determination methods. Thin Solid Films 669, 482–486. https://doi.org/10.1016/j.tsf.2018.11.017

Cojocaru-Mirédin, O., Raghuwanshi, M., Wuerz, R., Sadewasser, S., 2021. Grain Boundaries in Cu(In, Ga)Se2: A Review of Composition–Electronic Property Relationships by Atom Probe Tomography and Correlative Microscopy. Adv. Funct. Mater. 31. https://doi.org/10.1002/adfm.202103119

Curado, M.A., Teixeira, J.P., Monteiro, M., Ribeiro, E.F.M., Vilão, R.C., Alberto, H. V., Cunha, J.M.V., Lopes, T.S., Oliveira, K., Donzel-Gargand, O., Hultqvist, A., Calderon, S., Barreiros, M.A., Chiappim, W., Leitão, J.P., Silva, A.G., Prokscha, T., Vinhais, C., Fernandes, P.A., Salomé, P.M.P., 2020. Front passivation of Cu(In,Ga)Se2 solar cells using Al2O3: Culprits and benefits. Appl. Mater. Today 21. https://doi.org/10.1016/j.apmt.2020.100867

Czudek, A., Eslam, A., Urbaniak, A., Zabierowski, P., Wuerz, R., Igalson, M., 2020. Evolution of the electrical characteristics of Cu(In,Ga)Se2devices with sodium content. J. Appl. Phys. 128. https://doi.org/10.1063/5.0025183

de Wild, J., Birant, G., Eachambadi Thiruvallur, R., Kohl, T., Buldu, D.G., Brammertz, G., Manca, J. V., Meuris, M., Poortmans, J., Vermang, B., 2021. Detrimental impact of Na upon Rb post deposition treatments of Cu(In,Ga)Se 2 absorber layers Jessica de Wild. Sol. RRL. https://doi.org/10.1002/solr.202100390

de Wild, J., Buldu, D.G., Kohl, T., Birant, G., Brammertz, G., Meuris, M., Poortmans, J., Vermang, B., 2020. Intermediate scale bandgap fluctuations in ultrathin Cu(In,Ga)Se2 absorber layers. J. Appl. Phys. 128. https://doi.org/10.1063/5.0024840

de Wild, J., Buldu, D.G., Schnabel, T., Simor, M., Kohl, T., Birant, G., Brammertz, G., Meuris, M., Poortmans, J., Vermang, B., 2019. High Voc upon KF Post-Deposition Treatment for Ultrathin Single-Stage Coevaporated Cu(In, Ga)Se2 Solar Cells. ACS Appl. Energy Mater. 2. https://doi.org/10.1021/acsaem.9b01370

Eslam, A., Wuerz, R., Hauschild, D., Weinhardt, L., Hempel, W., Powalla, M., Heske, C., 2021. Impact of Substrate Temperature During NaF and KF Post-Deposition Treatments on Chemical and Optoelectronic Properties of Alkali-Free Cu(In,Ga)Se2 Thin Film Solar Cell Absorbers. Thin Solid Films 138979. https://doi.org/10.1016/j.tsf.2021.138979

Garud, S., Gampa, N., Allen, T.G., Kotipalli, R., Flandre, D., Batuk, M., Hadermann, J., Meuris, M., Poortmans, J., Smets, A., Vermang, B., 2018. Surface Passivation of CIGS Solar Cells Using Gallium Oxide. Phys. Status Solidi a 1700826, 1–6. https://doi.org/10.1002/pssa.201700826

Heise, S.J., López Salas, J.F., 2017. Charge separation effects in time-resolved photoluminescence of Cu(In,Ga)Se2 thin film solar cells. Thin Solid Films 633, 35–39. https://doi.org/10.1016/j.tsf.2016.11.031

Hultqvist, A., Sone, T., Bent, S.F., 2017. Buffer Layer Point Contacts for CIGS Solar Cells Using Nanosphere Lithography and Atomic Layer Deposition. IEEE J. Photovoltaics 7, 322–328. https://doi.org/10.1109/JPHOTOV.2016.2627621

Kandybka, I., Birant, G., De Wild, J., Buldu, D.G., Kohl, T., Thiruvallur Eachambadi, R., Brammertz, G., Manca, J. V., Meuris, M., Poortmans, J., Vermang, B., 2021. Novel cost-effective approach to produce nano-sized contact openings in an aluminum oxide passivation layer up to 30 nm thick for CIGS solar cells. J. Phys. D. Appl. Phys. 54. https://doi.org/10.1088/1361-6463/abed09

Kohl, T., Rivas, N.A., de Wild, J., Buldu, D.G., Birant, G., Brammertz, G., Meuris, M., Renner, F.U., Poortmans, J., Vermang, B., 2020. Inclusion of Water in Cu(In, Ga)Se 2 Absorber Material

During Accelerated Lifetime Testing . ACS Appl. Energy Mater. 3, 5120–5125. https://doi.org/10.1021/acsaem.0c00610

Lafuente-Sampietro, A., Yoshida, K., Wang, S., Ishizuka, S., Shibata, H., Sano, N., Akimoto, K., Sakurai, T., 2021. Effect of the double grading on the internal electric field and on the carrier collection in CIGS solar cells. Sol. Energy Mater. Sol. Cells 223, 110948. https://doi.org/10.1016/j.solmat.2020.110948

Li, W., Cohen, S.R., Cahen, D., 2014. Effect of chemical treatments on nm-scale electrical characteristics of polycrystalline thin film Cu(In,Ga)Se2 surfaces. Sol. Energy Mater. Sol. Cells 120, 500–505. https://doi.org/10.1016/j.solmat.2013.09.030

Li, Y., Yin, G., Gao, Y., Köhler, T., Lucaßen, J., Schmid, M., 2021. Sodium control in Ultrathin Cu(In,Ga)Se2 solar cells on transparent back contact for efficiencies beyond 12%. Sol. Energy Mater. Sol. Cells 223. https://doi.org/10.1016/j.solmat.2021.110969

Löckinger, J., Nishiwaki, S., Bissig, B., Degutis, G., Romanyuk, Y.E., Buecheler, S., Tiwari, A.N., 2019. The use of HfO 2 in a point contact concept for front interface passivation of Cu(In,Ga)Se 2 solar cells. Sol. Energy Mater. Sol. Cells 195, 213–219. https://doi.org/10.1016/j.solmat.2019.03.009

Lopes, T.S., De Wild, J., Rocha, C., Violas, A., Cunha, J.M.V., Teixeira, J.P., Curado, M.A., Oliveira, A.J.N., Borme, J., Birant, G., Brammertz, G., Fernandes, P.A., Vermang, B., Salomé, P.M.P., 2021. On the Importance of Joint Mitigation Strategies for Front, Bulk, and Rear Recombination in Ultrathin Cu(In,Ga)Se2Solar Cells. ACS Appl. Mater. Interfaces 13, 27713–27725. https://doi.org/10.1021/acsami.1c07943

Mollica, F., 2017. Optimization of ultra-thin Cu (In , Ga) Se2 based solar cells with alternative back-contacts.

Nakada, T., 2012. Invited Paper: CIGS-based thin film solar cells and modules: Unique material properties. Electron. Mater. Lett. 8, 179–185. https://doi.org/10.1007/s13391-012-2034-x

Nakamura, M., Yamaguchi, K., Kimoto, Y., Yasaki, Y., Kato, T., Sugimoto, H., 2019. Cd-Free Cu (In , Ga)(Se , S) 2 Thin-Film Solar Cell With Record Efficiency of 23 . 35 %. IEEE J. Photovoltaics 9, 1863–1867.

Ochoa, M., Buecheler, S., Tiwari, A.N., Carron, R., 2020. Challenges and opportunities for an efficiency boost of next generation Cu(In,Ga)Se2solar cells: Prospects for a paradigm shift. Energy Environ. Sci. 13, 2047–2055. https://doi.org/10.1039/d0ee00834f

Ohnesorge, B., Weigand, R., Bacher, G., Forchel, A., Riedl, W., Karg, F.H., 1998. Minority-carrier lifetime and efficiency of Cu(In,Ga)Se2 solar cells. Appl. Phys. Lett. 73, 1224–1226. https://doi.org/10.1063/1.122134

Park, J., Huang, J., Yun, J., Liu, F., Ouyang, Z., Sun, H., Yan, C., Sun, K., Kim, K., Seidel, J., Chen, S., Green, M.A., Hao, X., 2018. The Role of Hydrogen from ALD-Al2O3 in Kesterite Cu2ZnSnS4 Solar Cells: Grain Surface Passivation. Adv. Energy Mater. 8, 3–9. https://doi.org/10.1002/aenm.201701940

Pianezzi, F., Reinhard, P., Chirila, A., Bissig, B., Nishiwaki, S., Buecheler, S., Tiwari, A.N., 2014. Unveiling the effects of post-deposition treatment with different alkaline elements on the electronic properties of CIGS thin film solar cells. R. Soc. Chem. 16, 8843–8851. https://doi.org/10.1039/c4cp00614c

Puttnins, S., Hammer, M.S., Neerken, J., Riedel, I., Daume, F., Rahm, A., Braun, A., Grundmann, M., Unold, T., 2015. Impact of sodium on the device characteristics of low temperature-deposited Cu(In,Ga)Se2-solar cells. Thin Solid Films 582, 85–90. https://doi.org/10.1016/j.tsf.2014.07.048

Puttnins, S., Levcenko, S., Schwarzburg, K., Benndorf, G., Daume, F., Rahm, A., Braun, A., Grundmann, M., Unold, T., 2013. Effect of sodium on material and device quaility in low temperature deposited Cu(In,Ga)Se2. Sol. Energy Mater. Sol. Cells 119, 281–286.

Reinhard, P., Bissig, B., Pianezzi, F., Hagendorfer, H., Sozzi, G., Menozzi, R., Gretener, C., Nishiwaki, S., Buecheler, S., Tiwari, A.N., 2015. Alkali-templated surface nanopatterning of chalcogenide thin films: A novel approach toward solar cells with enhanced efficiency. Nano Lett. 15, 3334–3340. https://doi.org/10.1021/acs.nanolett.5b00584

Scaffidi, R., Buldu, D.G., Brammertz, G., de Wild, J., Kohl, T., Birant, G., Meuris, M., Poortmans, J., Flandre, D., Vermang, B., 2021. Comparative Study of Al 2 O 3 and HfO 2 for Surface Passivation of Cu(In,Ga)Se 2 Thin-Films: An Innovative Al 2 O 3 /HfO 2 Multi-Stack Design .

Phys. Status Solidi 2100073, 1–8. https://doi.org/10.1002/pssa.202100073

Scheer, R., Schock, H.-W., 2011. Chalcogenide Photovoltaics, Chalcogenide Photovoltaics. https://doi.org/10.1002/9783527633708

Shimakawa, S. ichi, Hashimoto, Y., Hayashi, S., Satoh, T., Negami, T., 2008. Annealing effects on Zn1-xMgxO/CIGS interfaces characterized by ultraviolet light excited time-resolved photoluminescence. Sol. Energy Mater. Sol. Cells 92, 1086–1090. https://doi.org/10.1016/j.solmat.2008.03.014

Shimakawa, S.I., Kitani, K., Hayashi, S., Satoh, T., Hashimoto, Y., Takahashi, Y., Negami, T., 2006. Characterization of Cu(In,Ga)Se 2 thin films by time-resolved photoluminescence. Phys. Status Solidi Appl. Mater. Sci. 203, 2630–2633. https://doi.org/10.1002/pssa.200669583

Shirakata, S., Nakada, T., 2007. Time-resolved photoluminescence in Cu (In , Ga) Se 2 thin films and solar cells. Thin Solid Films 515, 6151–6154. https://doi.org/10.1016/j.tsf.2006.12.040

Sozzi, G., Di Napoli, S., Menozzi, R., Bissig, B., Buecheler, S., Tiwari, A.N., 2017. Impact of front-side point contact/passivation geometry on thin-film solar cell performance. Sol. Energy Mater. Sol. Cells 165, 94–102. https://doi.org/10.1016/j.solmat.2017.02.031

Sozzi, G., Pignoloni, D., Menozzi, R., Pianezzi, F., Reinhard, P., Bissig, B., Buecheler, S., Tiwari, A.N., 2015. Designing CIGS solar cells with front-side point contacts. 2015 IEEE 42nd Photovolt. Spec. Conf. PVSC 2015 8–12. https://doi.org/10.1109/PVSC.2015.7355691

Vermang, B., Fjallström, V., Gao, X., Edoff, M., 2014. Improved rear surface passivation of Cu(In,Ga)Se2 solar cells: A combination of an Al2O3 rear surface passivation layer and nanosized local rear point contacts. IEEE J. Photovoltaics 4, 486–492. https://doi.org/10.1109/JPHOTOV.2013.2287769

Werner, F., Babbe, F., Burkhart, J., Conrad, S., Elanzeery, H., Siebentritt, S., 2018. Interdiffusion and Doping Gradients at the Buffer/Absorber Interface in Thin-Film Solar Cells. ACS Appl. Mater. Interfaces 10, 28553–28565.